Materials Science & Engineering A 802 (2021) 140637

Contents lists available at ScienceDirect

Materials Science & Engineering A

journal homepage: http://www.elsevier.com/locate/msea

Mechanical behaviors and precipitation transformation of the lightweight high-Zn-content Al–Zn–Li–Mg–Cu alloy

Ruixuan Li [a], Zheng Ren [b], Yuan Wu [a], Zhanbing He [a], Peter K. Liaw [c], Jingli Ren [d], Yong Zhang [a,e,*]

[a] Beijing Advanced Innovation Center for Materials Genome Engineering, State Key Laboratory for Advanced Metals and Materials, University of Science and Technology Beijing, Beijing, 100083, China
[b] Ningbo Branch of China Academy of Ordnance Science, Ningbo, China
[c] Department of Materials Science and Engineering, The University of Tennessee, Knoxville, TN, 37996, USA
[d] Henan Academy of Big Data, Zhengzhou University, Zhengzhou, 450001, China
[e] Qinghai Provincial Key Laboratory of New Light Alloys, Qinghai University, Xining, 810016, China

ARTICLE INFO

Keywords:
Al alloys
High entropy alloys
High Zn content
Precipitation strengthening
Precipitation transformation

ABSTRACT

Designing high-performance Al-based alloys based on the entropy concept offers a promising strategy for next-generation advanced structural materials. The main idea of entropy increasing is to increase the content of alloying elements. For traditional high-strength Al–Zn–Mg–Cu alloy, however, significantly increasing the content of alloying elements, especially when the Zn content is increased to above 10 at.% (atomic percent), leads to poor deformability and poor tensile property. Here, we overcome this trend by designing a quinary alloy based on the idea of high-entropy alloys. We fabricate a high-Zn-content $Al_{80}Zn_{14}Li_2Mg_2Cu_2$ alloy with the Zn content above 10 at.%. It shows Zn, and Al–Zn precipitates in the as-cast state, and it is observed that Al_3(Li, Mg), $MgZn_2$, and Zn nano-precipitates form after rolling. The precipitation transformation contributes to high strength and high deformability. Our present findings provide not only a fundamental understanding of precipitation transformation in the high-Zn-content Al alloys but valuable guidance for the development of lightweight alloys as well.

1. Introduction

High entropy alloys (HEAs) are usually defined as quinary alloys with high mixing entropy, and they have attracted much public concern for their outstanding mechanical properties [1–4], while the high density seriously hinders their application in lightweight fields, such as aerospace, automobile, and electronics [5,6]. Substituting light elements for heavy elements and developing lightweight HEAs are currently new research hotspots, such as the early AlNbTiV and $Al_{1.5}$CrFeMnTi alloy [7,8], which exhibit high compressive strength and great high-temperature properties. To further reduce the density, more and more lightweight main-group elements are added [9,10]. Due to the high electronegativity of main light elements and the strong interatomic interaction, bulk intermetallics appear in these as-cast lightweight HEAs. However, all these novel light alloys exhibit high compressive strength and considerable plasticity [11–14]. For example, the $Al_{15}Li_{39}Mg_{45}Ca_{0.5}Si_{0.5}$ alloy exhibits a compressive strength of more than 500 MPa and more than 60% plastic strain. Similarly, the compressive strength of the $Al_{80}Li_5Mg_5Zn_5Cu_5$ alloy even reaches 800 MPa, which has the plastic strain up to 17% [15,16].

For the traditional high strength Al–Zn–Mg–Cu alloys, although many trace elements are added to improve the comprehensive properties, the composition design range has remained almost unchanged for many years; that is, the mass fraction of Al is larger than 90 at.% (atomic percent), and that of each alloying element does not exceed 5 at.% [17–19]. The concept of entropy increasing provides a promising strategy for the development of novel Al alloys, and the research on lightweight HEAs has proved that high entropy can significantly improve the strength and the plasticity. Increasing the system entropy means increasing the content of alloying elements, and the increase of the Zn content in Al alloys has always been the focus of research. The slight increase of Zn to 5 at.% can effectively enhance the precipitation

* Corresponding author. Beijing Advanced Innovation Center for Materials Genome Engineering, State Key Laboratory for Advanced Metals and Materials, University of Science and Technology Beijing, Beijing, 100083, China.
E-mail address: drzhangy@ustb.edu.cn (Y. Zhang).

https://doi.org/10.1016/j.msea.2020.140637
Received 13 July 2020; Received in revised form 28 November 2020; Accepted 2 December 2020
Available online 5 December 2020

strengthening and increase the strength [20,21]. Then, a further increase of Zn to 10 at.% can contribute to high castability at the expense of strength and deformability. At this time, the composition moves to the eutectic point, and there are few precipitation strengthening effects [22,23].

A kind of novel $Al_{80}Li_5Mg_5Zn_5Cu_5$ alloy is prepared in our previous work, and significant-high compressive strength and plasticity are discovered [16]. In this paper, we further improve the Zn content to above 10 at.% and slightly adjust the content of other elements based on our previous alloy. We report a high-Zn-content $Al_{80}Zn_{14}Li_2Mg_2Cu_2$ alloy, which has the synergized tensile strength and ductility derived from the semi-coherent precipitation-hardening effect after rolling. These precipitates appear precisely in the equilibrium state, and their behaviors in different states, including morphology, composition, size, and density, are described carefully.

2. Experiment

The raw materials were pure aluminum [99.7 wt% purity (in weight percent)], pure zinc (99.9 wt% purity), magnesium-lithium alloys (Mg-20 wt% Li), and pure copper (99.9 wt% purity). The experimental alloys with a nominal chemical composition of $Al_{94-x}Zn_xLi_2Mg_2Cu_2$ (x = 5, 8, 11, 14, and 17 in at.%) were melted and cast into a water-cooled steel mold to prepare an ingot with the size of 170 mm (length) × 100 mm (width) × 100 mm (thickness). The compositional-optimized ingot of $Al_{80}Zn_{14}Li_2Mg_2Cu_2$ was cut into 20 mm-thick blocks. To obtain a dense block, the sampling position is selected at the side of the ingot near the bottom, as shown in Fig. 1(a). The block is then hot rolled from 20 mm to 4.0 mm at 350 °C, followed by the subsequent cold rolling to 1.5 mm at room temperature. That is to say, the hot rolling reduction ratio is about 80%, and the cold rolling reduction ratio is about 62.5%. The schematic of the cold-rolled plate is shown in Fig. 1(b).

Phase formation was determined by X-ray diffraction (XRD) on a Huber-2 goniometer (Cu-α radiation), followed by microstructural characterization using the scanning electron microscopy (SEM), energy dispersive spectrometry (EDS), and electron backscatter diffraction (EBSD). The precipitates were examined using the local electrode atom-probe tomography (LEAP 5000× SI), and the sharp atom-probe tomography (APT) tip was prepared employing the conventional Focused Ion Beam (FIB) milling process. The transmission electron microscopy (TEM) and selected area electron diffraction (SAED) operated at 300 kV were also conducted.

Mechanical properties of the alloy ingots and the cold-rolled plates were tested and compared. Room-temperature tensile and compressive properties were evaluated using a CMT4105 universal electronic tensile testing machine with an initial strain rate of $4 \times 10^{-4}\ s^{-1}$. Compression tests are performed on five alloy ingots to screen the best compositions. For the compositional-optimized $Al_{80}Zn_{14}Li_2Mg_2Cu_2$ alloy, the tensile properties of the ingots and the rolled plates were studied for comparison. The sampling positions, sample sizes, and cutting directions are shown in Fig. 1 (b) and (c).

3. Results

3.1. Microstructures and properties of the as-cast $Al_{94-x}Zn_xLi_2Mg_2Cu_2$ alloys

Fig. 2(a) shows XRD patterns of the as-cast $Al_{94-x}Zn_xLi_2Mg_2Cu_2$ (x = 5, 8, 11, 14, 17 in at.%) alloys, and inset is the enlarged pattern from 36° to 47° of 2θ when x = 17. Fig. 2(b) shows the corresponding compressive stress-strain curves. The diffraction peaks reveal the existence of α-Al, Al_5CuLi_3, Zn, and $MgZn_2$ phases. The characteristic peaks of these four phases stay almost the same in all alloys, suggesting nearly no phase transformation, while there is an increase in the diffraction intensity of both Al_5CuLi_3 and $MgZn_2$ phases when increasing Zn content. At the same time, the strength and plasticity undergo a rapid increase firstly and then decrease. That is to say, the increase of the intermetallics tends to strengthen the alloy, while the growth and coarsening of them will weaken this effect. The ultimate strength reaches its maximum at 1045 MPa when x = 14, along with a fracture strain of 22%. Therefore, the $Al_{80}Zn_{14}Li_2Mg_2Cu_2$ alloy is selected for further research.

The tensile stress-strain curves of the selected $Al_{80}Zn_{14}Li_2Mg_2Cu_2$ alloy in as-cast, hot-rolled, and cold-rolled states are further tested and plotted in Fig. 2(c). In contrast to other reported lightweight HEAs and high-Zn-content Al alloys that are prone to failure during deformation, the $Al_{80}Zn_{14}Li_2Mg_2Cu_2$ alloy achieves enhancement in strength and ductility simultaneously after hot rolling, which exhibits 450 MPa and 11%, respectively. The following cold rolling further increases the tensile strength to 603 MPa and retain more than 2% of plasticity, even if the cold rolling deformation ratio is up to 62.5%.

To emphasize the substantial improvement in the mechanical properties, we compare our designated alloy to some other similar Al-based alloys reported in the literature (Please find Fig. 2(d) and Table S1 for more detail). Here, the high-Zn-content Al alloys include Al alloys with Zn content larger than 10 at.%. In terms of the compressive properties, the as-cast $Al_{80}Zn_{14}Li_2Mg_2Cu_2$ alloy shows the best strength-density combination when compared with other reported lightweight HEAs and Al-based bulk metallic glasses (BMGs). Moreover, unlike the micron size scale of Al-based BMGs, our alloy has no size limitation, which is conducive to large-scale preparation in practical application. In terms of the tensile properties, compared with the high-Zn-content Al alloys, which have tensile strength smaller than 500 MPa, our alloy also

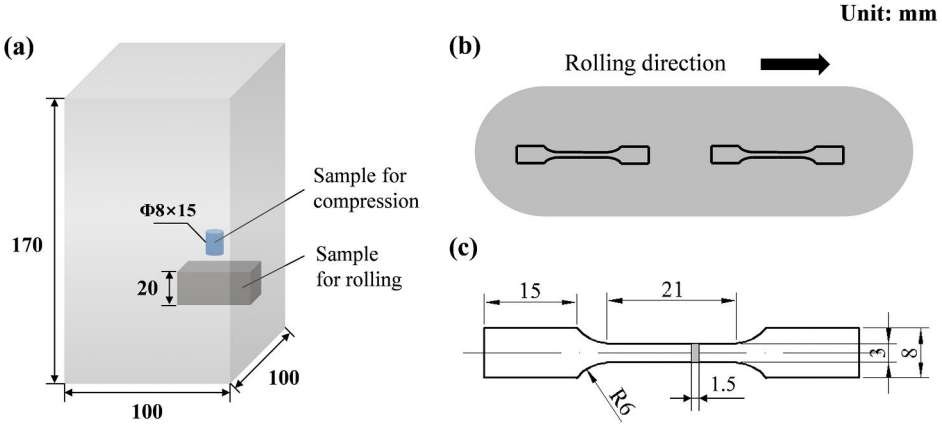

Fig. 1. Schematic of the sampling positions, sample sizes, cutting direction, and the stress axis direction in the experiment. (a) Sampling positions and sample sizes in the original ingot. (b) Schematic of the rolled plate and the sampling position for tensile testing. (c) The sampling dimension for the tensile testing.

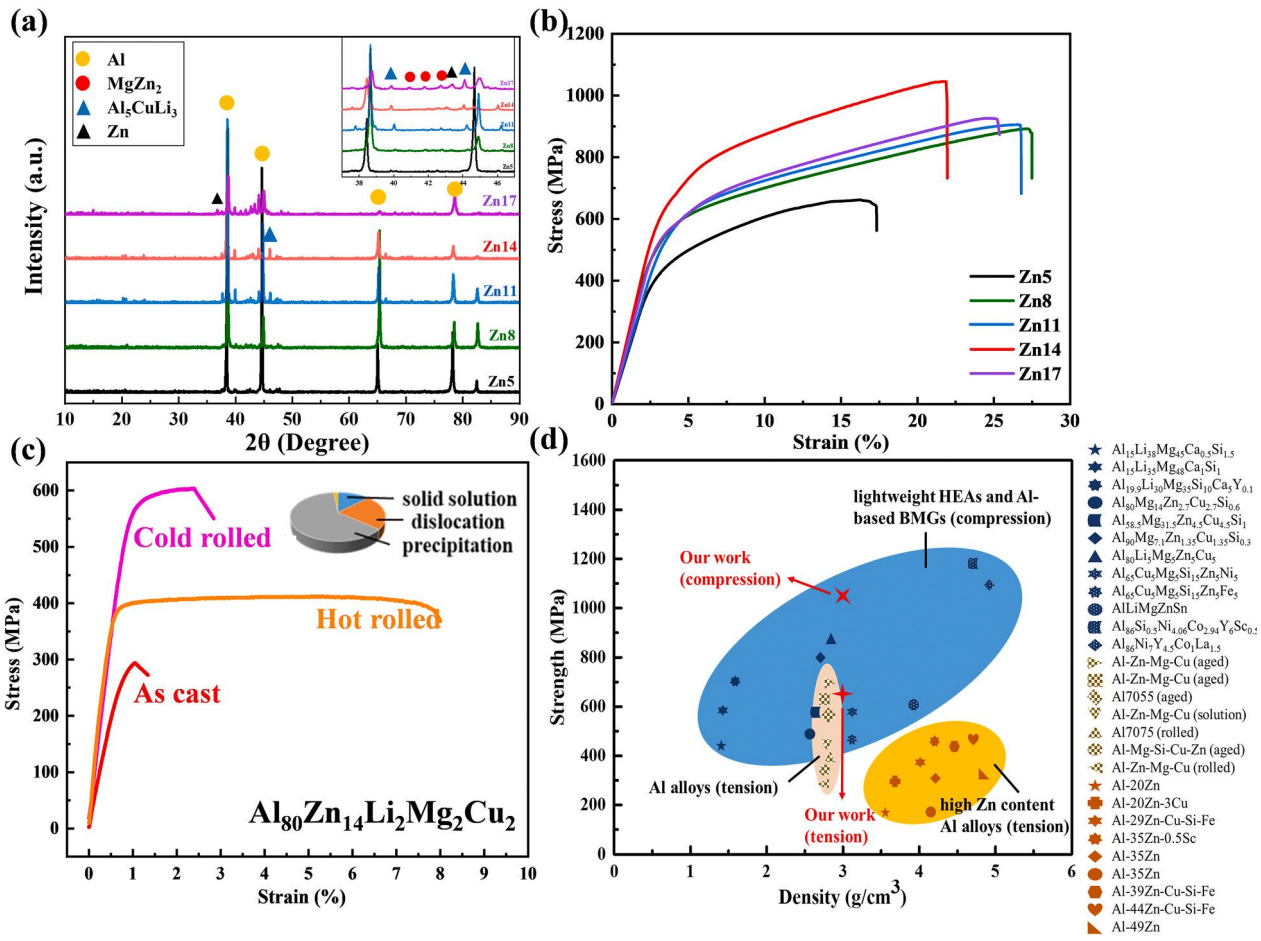

Fig. 2. Phase structures and properties of $Al_{94-x}Zn_xLi_2Mg_2Cu_2$ (x = 5, 8, 11, 14, and 17 in at.%) alloys. (a) XRD patterns and (b) the compressive stress-strain curves of as-cast $Al_{94-x}Zn_xLi_2Mg_2Cu_2$ alloys. (c) The tensile stress-strain curves of the as-cast, hot-rolled, and cold-rolled $Al_{80}Zn_{14}Li_2Mg_2Cu_2$ alloy. The inset pie chart describes the main strengthening contributions of the cold-rolled alloy. (d) The comparison of the density and strength between some similar Al-based alloys and the $Al_{80}Zn_{14}Li_2Mg_2Cu_2$ alloy in the present work.

exhibits a significantly enhanced strength. Its deformed tensile performance is at the same level as the aged high-strength Al–Zn–Mg–Cu alloys, suggesting our alloy is capable of breaking the limitation of the existing high-Zn-content Al alloys and expanding its application prospects to structural materials.

3.2. Microstructures of the as-cast $Al_{80}Zn_{14}Li_2Mg_2Cu_2$ alloy

The SEM image of the as-cast $Al_{80}Zn_{14}Li_2Mg_2Cu_2$ alloy presented in Fig. 3(a) indicates the formation of a dendritic structure, whose detailed composition is obtained through EDS (Table S2). Combined with the XRD data, the gray and white contrast areas are identified as Al_5CuLi_3 and $MgZn_2$ phases, respectively. The Al_5CuLi_3 phase, confirmed by the SAED, reveals its body-centered-cubic (BCC) structure with a lattice constant a = b = c = 1.39 nm. A representative bright-field TEM image taken from the dark contrast (the Al phase) of SEM [Fig. 3(b)] gives a general view of two kinds of precipitates, including rod-shaped ones with the length of several hundred nanometers and inhomogeneous spherical clusters with the diameter of about 60 nm. The rod-shaped precipitates have an ellipse cross-section with a size of about 20 × 100 nm, and they distribute along the <111> axis of Al, which has the lowest distortion energy [24]. The high-resolution TEM image of the rod-shaped precipitates shown in Fig. 3(c) indicates these precipitates have BCC structures with a lattice constant equal to 11.8 Å, and the orientation relationship is $(01\bar{1})$Al–Zn//(200)Al and $(2\bar{1}1)$Al–Zn//$(11\bar{1})$Al.

The APT analysis is performed to compare the composition of these two precipitates. The result is shown in Fig. 3(d), (e), and (f), and they indicate that the five raw elements, Al, Li, Mg, Zn, and Cu, exist in all precipitates and only differ in concentration according to their shapes. Precipitates with similar forms share a similar composition. The Al/Zn concentration of the rod-shaped and the spherical precipitates are found to be 71.8 at.%/20.6 at.% and 4 at.%/76 at.%, respectively, and other three elements Li, Mg, and Cu are only slightly enriched in the precipitates. Therefore, the rod-shaped precipitates are characterized as the Al–Zn phase, and the spherical ones are Zn phases.

3.3. Microstructures of the deformed $Al_{80}Zn_{14}Li_2Mg_2Cu_2$ alloy

The long rod-shaped precipitates usually cause the appearance and propagation of cracks during deformation, and the inhomogeneous-distributed spherical precipitates retard the potential to effectively strengthening. Thus, the as-cast alloy is further deformed to develop modified microstructure and precipitation.

After hot rolling, the EBSD inverse pole figure (IPF) in Figure S1(a) indicates that the microstructure is almost fully recrystallized with randomly-oriented and equiaxed grains. The TEM image in Figure S1(b) shows that dislocation lines can be seen in only a few areas in the sample. As a result, the alloy has a low initial dislocation density. As exhibited in Fig. 4(a1), no phase transformation occurs after hot rolling, and three phases, α-Al, Al_5CuLi_3, and $MgZn_2$, are still visible, as confirmed by the XRD results (Figure S2). The main difference is that the coarse dendrites in the as-cast state are crushed by shear stresses during

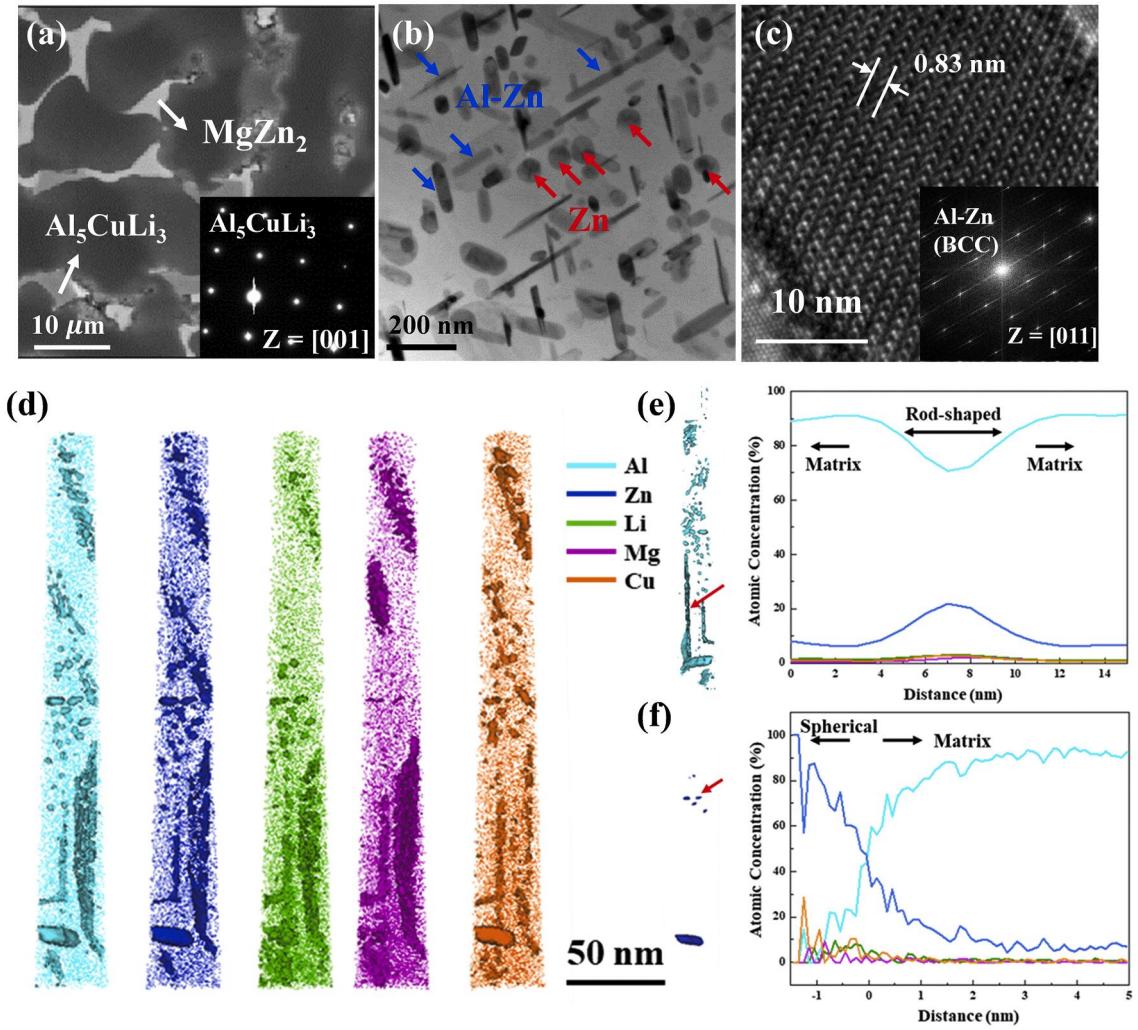

Fig. 3. Microstructures and precipitates of the as-cast $Al_{80}Zn_{14}Li_2Mg_2Cu_2$ alloy. (a) The SEM image of the alloy. (b) The bright-field TEM image taken from the Al phase. (c) The high-resolution TEM image of the Al–Zn rod-shaped precipitates. Inset is the corresponding FFT image showing its BCC structure. (d) 75Al, 20Zn, 2.5Li, 1.5 Mg, 2.5Cu (at.%) isoconcentration surface for the as-cast sample. (e) Proximity histogram based on the 75 at.% Al isoconcentration surface showing the composition change across the arrowed rod-shaped precipitates. (f) Proximity histogram based on the 40 at.% Zn isoconcentration surface presenting the compositional change across the arrowed spherical precipitates.

deformation, and the particles are generally oriented in the direction of the metal flow. The size of Al_5CuLi_3 is decreased to about several tens of micrometers, while some $MgZn_2$ phases are even fractured into micro- or nano-meters when the applied internal stress exceeds their fracture stress [21].

As shown in Fig. 4(b1), the nano-scaled structures taken from the Al phase also undergo visible changes compared with the as-cast alloy, where the precipitation density sharply decreases, and all the precipitates change into spherical or small needle-like shapes. Through the characterization by TEM-EDS, the spherical nano-particles located in grain interiors are identified as Zn and $MgZn_2$ with a mean diameter of 150 nm and 300 nm, respectively. The average diameter of needle-shaped ones is estimated at 100 nm, and they are enriched with Al and Mg with an atomic ratio of 3:1 (The detailed compositions from two representative particles are listed in Table S3). However, previous experimental observations proved that the metastable $L1_2$ Al_3Mg phase (β'') only could appear in Al alloys, which contain high levels of Mg (>10 at.%) [25], while the alloy composition that we designed is far from this requirement. On the other hand, considering that the atomic content of Li cannot be detected by EDS and the similarity of the atomic radii between Mg and Li, it can be assumed that the Al_3(Mg, Li) phase with an $L1_2$ structure is formed due to the elemental replacement.

The microstructure of the alloy after cold rolling is shown in Fig. 4 (a2) and (b2), and no phase transformation occurs, as confirmed by the XRD patterns in Figure S2. Fig. 4(a2) exhibits that both $MgZn_2$ and Al_5CuLi_3 are further crushed and distribute along the rolling direction. As shown in Fig. 4(b2), in terms of nano-scale structures in the Al phase, spherical Zn and needle-like Al_3(Li, Mg) precipitates remain the same, but their density and size undergo significant change, compared with the hot-rolled alloy. The area fraction of Zn particles sharply increases by 9 times, and their average diameter decreases from 150 nm to 40 nm. The area fraction of the Al_3(Li, Mg) phase is enhanced from 3% to 6%, and their average diameter even obviously decreases by 90%. The types, sizes, and area fractions of the precipitates in the as-cast, hot-rolled, and cold-rolled alloy states are shown in Table 1 in detail. The bright-field TEM micrograph of the cold-rolled plate is shown in Figure S3 of the Supplementary Material. The dislocation density is estimated at 8×10^{14} m^{-2} and is consistent with other work in which alloys are subjected to 60% cold-rolling deformation [26].

In Fig. 4(c), (d), and (e), structures of these three nano phases are further analyzed using the representative bright-field TEM image and the high-resolution TEM. The fast Fourier transform (FFT) image in Fig. 4(c) indicates the (100) atomic planes of Al_3(Li, Mg) and confirms the $L1_2$-structure with a lattice constant of about 0.46 nm. There is also a

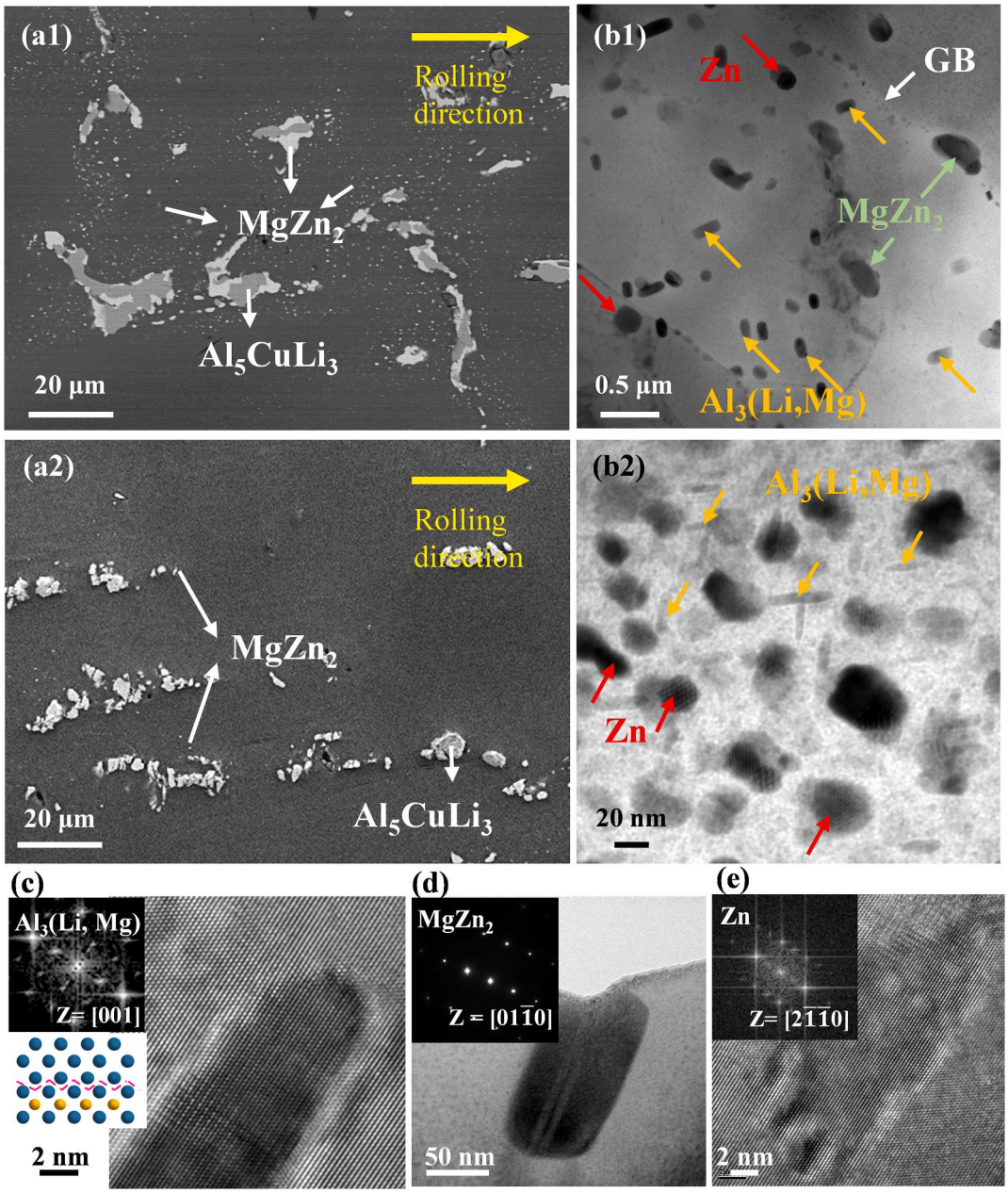

Fig. 4. Microstructures and precipitations of the hot-rolled and cold-rolled $Al_{80}Zn_{14}Li_2Mg_2Cu_2$ alloy. (a1) The SEM and (b1) bright-field TEM image after hot rolling. GB is the grain boundary. (a2) The SEM and (b2) the bright-field TEM image after cold rolling. (c) The high-resolution TEM and the corresponding FFT image of a nano Al_3(Li, Mg) particle. Inset is the schematic illustration revealing the interfacial coherence between the particle and matrix. (d) The bright-field TEM and SAED image of an $MgZn_2$ particle. (e) The high-resolution TEM image of a nano Zn particle and the inset is the FFT image.

Table 1
The types, sizes, and area percentages of the precipitates in the as-cast, hot-rolled, and cold-rolled states of $Al_{80}Zn_{14}Li_2Mg_2Cu_2$ alloy. Over 50 different nano-particles were used in determining these parameters.

	Precipitation	Mean radius (nm)	Mean length (nm)	Fraction (%)
As cast	Zn	62	/	5
	Al–Zn	20 × 100 (ellipse)	730	11
Hot rolled	$MgZn_2$	300	/	2
	Zn	150	/	1
	Al_3(Li, Mg)	100	200	3
Cold rolled	$MgZn_2$	200–300	/	3
	Zn	40	/	9
	Al_3(Li, Mg)	10	50	6

semi-coherent relationship between (111)Al and (200)Al_3(Mg, Li) planes, and the inset schematic illustration clearly reveals this interfacial coherence. The size of nano-scale $MgZn_2$ is relatively large owing to the stress breakage during rolling, and SAED confirms its hexagonal close-packed (HCP) structure. The spherical nano-Zn precipitates with HCP structures have a semi-coherent relationship with the (111)Al matrix plane because of similar d-spacing values (~0.24 nm) of (0002) Zn and (111)Al.

4. Discussion

4.1. Precipitation transformation

Along with the change of properties in different alloy states, different precipitation phases appear on the Al matrix. Based on the APT and TEM

results, our view of the precipitation transformation is schematically shown in Fig. 5.

In Fig. 5(a), as the solid solubility decreases rapidly with the temperature decrease, supersaturated Zn atoms tend to precipitate into spherical nanoparticles in the α-Al solid solution [22]. The formation of long rod-shaped Al–Zn precipitates is due to the non-equilibrium solidification. The designed composition with the high Zn content is close to the eutectic point, and the complex interactions among various alloying elements may result in a chemical ordering in the melt, both of which ultimately reduce the free energy of the melt and increase the supercooling degree [27]. Miller et al. [24] confirmed that the temperature-influenced strain energy and chemical energy during solidification have significant effects on the morphology of the Al–Zn precipitates: the former is platelet-stabilizing, and the latter leads to a more spherical shape. As the chemical energy decreases rapidly with temperature, the strain energy dominates due to the increased supercooling degree, and eventually, a long rod-shaped Al–Zn precipitate is generated in the alloy.

Fig. 5(b) exhibits the equilibrium state in hot-rolled alloys. The growth and coarsening of precipitates are thermodynamically enhanced by the rolling heat and are kinetically supported by the highly-abundant defects. Thus, because of the high diffusion rates of Zn atoms, the average diameter of nano Zn particles increases, and some of them tend to aggregate in the grain boundaries. In terms of the formation of Al_3(Li, Mg) precipitates, in Al–Li–Mg alloys, Mg seems to greatly enhance the precipitation of Al_3Li in comparison to that observed in the Al–Li binary system. Gault et al. [28] proved that it is a favorable energetic situation, which enhances the Mg partition to the Li sites within the Al_3Li precipitates.

As shown in Fig. 5(c), when the alloy is then cold-rolled under the external force, various phases are further broken, sizes are reduced, and the defect density is rapidly increased, including vacancies and dislocations. As Li atoms have the most substantial binding energy with vacancies [29], the density of Li-containing precipitates increases under this driving force. However, because the atomic percentage of Li is not high enough, it cannot completely inhibit the diffusion of Zn atoms. Zn atoms are also bound to vacancies, and the final precipitation density is increased. Eventually, an ideal multi-phase microstructure, i.e., high-density nano-sized $L1_2$ and HCP phases semi-coherently disperse in the FCC matrix, can be suggested with a high probability of success.

4.2. Relationship between microstructures and properties

Considering the nature of this precipitation-strengthened alloy, the influence of grain refinement, and the plastic deformation during rolling, the following strengthening mechanisms need to be investigated to explain the higher strength in the cold-rolled alloy: grain-boundary strengthening, solid-solution strengthening, dislocation strengthening, and precipitation strengthening. Quantitative estimates of the contributions are described below, and the strength increments stemming from the four mechanisms are summarized in Fig. 2(c).

One of the most significant consequences of hot rolling is the grain-size refinement, creating a high volumetric density of grain boundaries that impede dislocation movement and dislocation propagation to adjacent grains, thereby strengthening the materials. The grain-boundary strengthening mechanism is usually described by the Hall-Petch equation [30]:

$$\Delta\sigma_{GB} = \mathrm{k}d^{-1/2} \tag{1}$$

Here k is the Hall-Petch coefficient equal to 0.12 MPa $m^{1/2}$ for Al-based alloys [31]. d is the average grain size of about 100 μm, which is estimated from Figure S1 by averaging the length and the width of the elongated grains. Therefore, the increase in strength due to grain-boundary strengthening is calculated as about only 10 MPa. It is clear that because of the sizeable micron-scale grain size, the grain-boundary strengthening effect is weak.

There is a considerable solid-solution strengthening in this alloy, for the variation of strain fields caused by the high Zn alloying elements [32]. The local strain field has a strong interaction with dislocations and can effectively impede their motion. Different atoms with various radii contribute differently to the local strain field and thus to the strength. Hence, the solid solution strengthening can be estimated as [33]:

$$\Delta\sigma_{ss} = \sum \Delta\sigma_i c_i \tag{2}$$

where $\Delta\sigma_i$ and c_i are the theoretical strengthening contribution and the fraction of each element, respectively. The $\Delta\sigma_i$ of Zn, Cu, and Mg to the yield strength is regarded as 2.9, 13.8, and 18.6 MPa/wt.%, respectively [33], and the weight percent of them are 22.1, 2.36, and 0.35 wt%, respectively, which are detected by SEM-EDS of cold-rolled alloys. The calculated hardening value is 103 MPa. Considering that Mg, Zn, and Cu

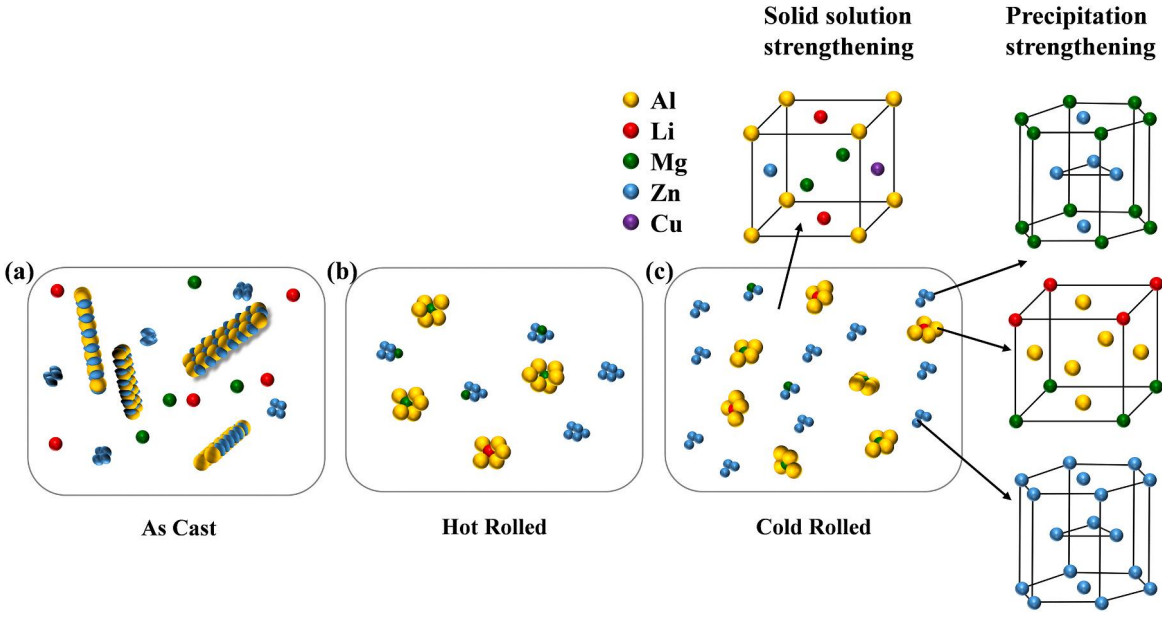

Fig. 5. Schematic illustration of precipitation transformation. (a) As-cast, (b) hot-rolled, and (c) cold-rolled state. Strengthening mechanisms from the solid solution and precipitation are also shown in (c).

are not all in solid solutions because they form precipitates or segregate to the grain boundaries, the actual strength increase from solution strengthening is relatively smaller.

The dislocation density significantly increases during cold rolling, and the subsequent interactions impede their own motion. Furthermore, the geometrically-necessary boundaries and rolling textures also contribute to the strength increase. The strength increase from dislocation strengthening can be calculated through [33].

$$\Delta\sigma_D = MaGb\rho^{1/2} \tag{3}$$

where M is the Taylor factor equal to 3.06 for the face-centered-cubic alloy; a is a constant equal to 0.2; G is the shear modulus equal to 27 GPa for Al-based alloys; b is the value of the Burgers vector (0.286 nm for Al), and ρ is the dislocation density, which is determined by TEM (Figure S3). Therefore, the strength increment caused by the dislocation density is calculated to be about 140 MPa.

Clearly, the above three strengthening methods provide a small increase in strength. Precipitation strengthening is supposed to play the most significant role in the final strength increment when considering the high-density nano-precipitates in the cold-rolled alloy. Dislocations interact with nanoparticles in two ways, namely the shearing mechanism and the Orowan bypass mechanism [34]. In general, the former will be active when the precipitate is small and coherent, while the latter occurs preferentially when the precipitate is copious or incoherent. Considering that the three precipitated phases are semi-coherent or incoherent with the matrix, we decide to use the Orowan mechanism to estimate the strengthening contribution from nanoparticles, which can be calculated as [33].

$$\Delta\sigma_{Orowan} = \frac{0.4MGb}{\pi\sqrt{1-\nu}}\frac{\ln(2\bar{r}/b)}{L_p} \tag{4}$$

where ν is the Poisson ratio (0.33 for Al), L_p is the interparticle distance, and $\bar{r} = \sqrt{2/3}r$. Here, r is the mean radius of the precipitates, and the relationship among the precipitation fraction f, L_p, and $\bar{r}$ is established as $L_p = 2\bar{r}(\sqrt{\pi/4f} - 1)$. It is evident that the strength increment originated from the Orowan mechanism is only dependent on r and L_p and is independent of the intrinsic properties of the precipitates, e.g., the chemical composition and crystal structure. Assuming that all the precipitates are spherical, and the types and sizes of the precipitates in the as-cast, hot-rolled, and cold-rolled states of $Al_{80}Zn_{14}Li_2Mg_2Cu_2$ are shown in Table 1 in detail. Therefore, the calculated value is 380 MPa.

The contributions from the four different strengthening mechanisms are added linearly, and the calculated overall strength is about 639 MPa, which is slightly larger than the experimental yield strength of 580 MPa. We speculate that the overestimate may come from the high-density nanoprecipitation, which results in the actually-weak solid-solution hardening. Furthermore, a fraction of the precipitates is located on the grain boundaries, while we assume that all precipitates are situated in grain interiors. The estimated strength increment for different strengthening mechanisms is shown in the pie chart inside Fig. 2(c). It is clear that the contribution of nano-precipitation strengthening to strength is the largest, accounting for more than 50%, followed by a work-hardening effect. That is to say, designing high-density nano-precipitation in the matrix is an effective way to enhance both the strength and ductility in the Al-based alloys.

5. Conclusion

In the present work, we have borrowed the design ideas of quinary HEAs and the method of entropy increasing and fabricated a new precipitation-hardened quinary $Al_{80}Zn_{14}Li_2Mg_2Cu_2$ alloy with synergetic strength and ductility. The conclusions are as follows:

A series of Al–Zn–Li–Mg–Cu alloys with increased Zn content is designed and screened. The compositional-optimized $Al_{80}Zn_{14}Li_2Mg_2Cu_2$ alloy exhibits high compressive strength (more than 1 GPa) and high plasticity (more than 20%) in the as-cast state. After rolling, it achieves similar strength levels to high-strength Al alloys, and it shows a considerable ductility. As a result, our alloy can break the limitation of current lightweight HEAs and high-Zn-content Al alloys and expand its application prospects to structural materials.

The spherical pure Zn and long rod-shaped Al–Zn particles are present in the as-cast alloy due to the solubility change and the non-equilibrium solidification process, followed by the transformation of spherical and needle-shaped particles after hot rolling. This precipitation transformation contributes to high strength and high deformability. Then, in the cold-rolled alloy, the increase in defect density drives the size and density of the nano-precipitated phase to decrease further. These high-density precipitates lead to the dominant strengthening effect, accounting for more than 50% of the total strength.

Data availability

We are ready to share all the raw data generated as part of the present study if a request comes from the scientific audience with appropriate reasons and intent.

CRediT authorship contribution statement

Ruixuan Li: Methodology, Investigation, Writing - original draft. **Zheng Ren:** Resources, Writing - review & editing. **Yuan Wu:** Investigation, Writing - review & editing. **Zhanbing He:** Investigation, Writing - review & editing. **Peter K. Liaw:** Writing - review & editing. **Jingli Ren:** Formal analysis, Writing - review & editing. **Yong Zhang:** Conceptualization, Methodology, Supervision, Project administration.

Declaration of competing interest

The authors declare that they have no known competing financial interests or personal relationships that could have appeared to influence the work reported in this paper.

Acknowledgements

R.X. Li would like to thank the useful help from Y.S. Li and H.K Ma in the experiment. Y. Zhang would like to thank the financial support from the National Science Foundation of China (Grant No. 51671020), and the project of Al–Mg based medium-entropy alloys with Dongguan Eontec company. Y. Zhang would also like to thank the financial support from the Fundamental Research Funds for the Central Universities (Grant Nos. FRF-MP-19-013 and 2020Z-08). Z.B. He would like to thank the financial support from the National Science Foundation of China (Grant No. 51871015). P.K.L. thanks the National Science Foundation DMR-1611180 and 1809640 with program directors, Drs. J. Yang, G. Shiflet, and D. Farkas. P.K.L. appreciates the support from the US Army Research Office Project nos. W911NF-13–1-0438 and W911NF-19–2-0049 with program managers, Drs. M.P. Bakas, S.N. Mathaudhu, and D. M. Stepp. J.L. Ren would like to thank the financial support from the National Science Foundation of China (Grant No. 11771407).

Appendix A. Supplementary data

Supplementary data to this article can be found online at https://doi.org/10.1016/j.msea.2020.140637.

References

[1] Z. Fu, L. Jiang, J.L. Wardini, B.E. MacDonald, H. Wen, W. Xiong, D. Zhang, Y. Zhou, T.J. Rupert, W. Chen, E.J. Lavernia, A high-entropy alloy with hierarchical nanoprecipitates and ultrahigh strength, Sci. Adv. 4 (2018) eaat8712.

[2] B. Gludovatz, A. Hohenwarter, D. Catoor, E.H. Chang, E.P. George, R.O. Ritchie, A fracture-resistant high-entropy alloy for cryogenic applications, Science 345 (2014) 1153–1158.
[3] Z. Zhang, M.M. Mao, J. Wang, B. Gludovatz, Z. Zhang, S.X. Mao, E.P. George, Q. Yu, R.O. Ritchie, Nanoscale origins of the damage tolerance of the high-entropy alloy CrMnFeCoNi, Nat. Commun. 6 (2015) 10143.
[4] Q. Ding, Y. Zhang, X. Chen, X. Fu, D. Chen, S. Chen, L. Gu, F. Wei, H. Bei, Y. Gao, M. Wen, J. Li, Z. Zhang, T. Zhu, R.O. Ritchie, Q. Yu, Tuning element distribution, structure and properties by composition in high-entropy alloys, Nature 574 (2019) 223–227.
[5] T.M. Pollock, Alloy design for aircraft engines, Nat. Mater. 15 (2016) 809–815.
[6] W.S. Miller, L. Zhuang, J. Bottema, A.J. Wittebrood, P. De Smet, A. Haszler, A. Vieregge, Recent development in Aluminium alloys for the automotive industry, Mater. Sci. Eng. A 280 (2000) 37–49.
[7] R. Feng, M.C. Gao, C. Zhang, W. Guo, J.D. Poplawsky, F. Zhang, J.A. Hawk, J. C. Neuefeind, Y. Ren, P.K. Liaw, Phase stability and transformation in a light-weight high-entropy alloy, Acta Mater. 146 (2018) 280–293.
[8] N.D. Stepanov, D.G. Shaysultanov, G.A. Salishchev, M.A. Tikhonovsky, Structure and mechanical properties of a light-weight AlNbTiV high entropy alloy, Mater. Lett. 142 (2015) 153–155.
[9] Y. Zhang, T.T. Zuo, Z. Tang, M.C. Gao, K.A. Dahmen, P.K. Liaw, Z.P. Lu, Microstructures and properties of high-entropy alloys, Prog. Mater. Sci. 61 (2014) 1–93.
[10] Y. Zhang, High-entropy Materials: A Brief Introduction, Springer, Singapore, 2019.
[11] E.J. Baek, T.Y. Ahn, J.G. Jung, J.M. Lee, Y.R. Cho, K. Euh, Effects of ultrasonic melt treatment and solution treatment on the microstructure and mechanical properties of low-density multicomponent Al70Mg10Si10Cu5Zn5 alloy, J. Alloys Compd. 696 (2017) 450–459.
[12] L. Shao, T. Zhang, L. Li, Y. Zhao, J. Huang, P.K. Liaw, Y. Zhang, A low-cost lightweight entropic alloy with high strength, J. Mater. Eng. Perform. 27 (2018) 6648–6656.
[13] K.K. Tseng, Y.C. Yang, C.C. Juan, T.S. Chin, C.W. Tsai, J.W. Yeh, A light-weight high-entropy alloy Al20Be20Fe10Si15Ti35, Sci. China Technol. Sci. 61 (2018) 184–188.
[14] Y. Li, R. Li, Y. Zhang, Effects of Si addition on microstructure, properties and serration behaviors of lightweight Al-Mg-Zn-Cu medium-entropy alloys, Research and Application of Materials Science 1 (2019) 10–17.
[15] Y. Jia, Y. Jia, S. Wu, X. Ma, G. Wang, Novel ultralight-weight complex concentrated alloys with high strength, Materials 12 (2019) 1136.
[16] X. Yang, S.Y. Chen, J.D. Cotton, Y. Zhang, Phase stability of low-density, multiprincipal component alloys containing Aluminum, Magnesium, and Lithium, JOM 66 (2014) 2009–2020.
[17] Q. Zhu, L. Cao, X. Wu, Y. Zou, M.J. Couper, Effect of Ag on age-hardening response of Al-Zn-Mg-Cu alloys, Mater. Sci. Eng. A 754 (2019) 265–268.
[18] Y. Zhang, S. Jin, P.W. Trimby, X. Liao, M.Y. Murashkin, R.Z. Valiev, J. Liu, J. M. Cairney, S.P. Ringer, G. Sha, Dynamic precipitation, segregation and strengthening of an Al-Zn-Mg-Cu alloy (AA7075) processed by high-pressure torsion, Acta Mater. 162 (2019) 19–32.
[19] H. Zhao, F. De Geuser, A. Kwiatkowski da Silva, A. Szczepaniak, B. Gault, D. Ponge, D. Raabe, Segregation assisted grain boundary precipitation in a model Al-Zn-Mg-Cu alloy, Acta Mater. 156 (2018) 318–329.
[20] K. Wen, Y. Fan, G. Wang, L. Jin, X. Li, Z. Li, Y. Zhang, B. Xiong, Aging behavior and precipitate characterization of a high Zn-containing Al-Zn-Mg-Cu alloy with various tempers, Mater. Des. 101 (2016) 16–23.
[21] W. Feng, X. Baiqing, Z. Yongan, L. Hongwei, L. Zhihui, L. Qiang, Microstructure and mechanical properties of spray-deposited Al-Zn-Mg-Cu alloy processed through hot rolling and heat treatment, Mater. Sci. Eng. A 518 (2009) 144–149.
[22] H.J. Jiang, C.Y. Liu, Y. Chen, Z.X. Yang, H.F. Huang, L.L. Wei, Y.B. Li, H.Q. Qi, Evaluation of microstructure, damping capacity and mechanical properties of Al-35Zn and Al-35Zn-0.5Sc alloys, J. Alloys Compd. 739 (2018) 114–121.
[23] W.B. Zhou, G.B. Teng, C.Y. Liu, H.Q. Qi, H.F. Huang, Y. Chen, H.J. Jiang, Microstructures and mechanical properties of binary Al-Zn alloys fabricated by casting and heat treatment, J. Mater. Eng. Perform. 26 (2017) 3977–3982.
[24] S. Müller, C. Wolverton, L.W. Wang, A. Zunger, Predicting the size-and temperature-dependent shapes of precipitates in Al-Zn alloys, Acta Mater. 48 (2000) 4007–4020.
[25] M. Satrink, A.M. Zahra, The kinetics of isothermal β′ precipitation in Al-Mg alloys, J. Mater. Sci. 34 (1999) 1117–1127.
[26] S.C. Wang, Z. Zhu, M.J. Starink, Estimation of dislocation densities in cold rolled Al-Mg-Cu-Mn alloys by combination of yield strength data, EBSD and strength models, J. Microsc. 217 (2005) 174–178.
[27] G. Chen, X. Hui, S. Fan, H. Kou, K. Yao, Concept of chemical short range order domain and the glass forming ability in multicomponent liquid, Intermetallics 10 (2002) 1221–1232.
[28] B. Gault, X.Y. Cui, M.P. Moody, F. De Geuser, C. Sigli, S.P. Ringer, A. Deschamps, Atom probe microscopy investigation of Mg site occupancy within δ′ precipitates in an Al-Mg-Li alloy, Scripta Mater. 66 (2012) 903–906.
[29] C. Wolverton, Solute-vacancy binding in aluminum, Acta Mater. 55 (2007) 5867–5872.
[30] C.S. Pande, K.P. Cooper, Nanomechanics of Hall-Petch relationship in nanocrystalline materials, Prog. Mater. Sci. 54 (2009) 689–706.
[31] K. Ma, T. Hu, H. Yang, T. Topping, A. Yousefiani, E.J. Lavernia, J.M. Schoenung, Coupling of dislocations and precipitates: impact on the mechanical behavior of ultrafine grained Al-Zn-Mg alloys, Acta Mater. 103 (2016) 153–164.
[32] R.L. Fleischer, Solution hardening by tetragonal distortions: application to irradiation hardening in fcc crystals, Acta Metall. 10 (1962) 835–842.
[33] K. Ma, H. Wen, T. Hu, T.D. Topping, D. Isheim, D.N. Seidman, E.J. Lavernia, J. M. Schoenung, Mechanical behavior and strengthening mechanisms in ultrafine grain precipitation-strengthened Aluminum alloy, Acta Mater. 62 (2014) 141–155.
[34] A.W. Zhu, E.A. Starke Jr., Strengthening effect of unshearable particles of finite size: a computer experimental study, Acta Mater. 47 (1999) 3263–3269.